

Ultraviolet photon production rates of the first stars: Impact on the He II λ 1640 Å emission line from primordial star clusters and the 21-cm signal from cosmic dawn

Joel Wasserman,¹ Erik Zackrisson,¹ [★] Jiten Dhandha,² Anastasia Fialkov,² Leon Noble,³ Suman Majumdar³

¹*Observational Astrophysics, Department of Physics and Astronomy, Uppsala University, Box 516, SE-751 20 Uppsala, Sweden*

²*Institute of Astronomy, University of Cambridge, Madingley Road, Cambridge, CB3 0HA, UK*

³*Department of Astronomy, Astrophysics & Space Engineering, Indian Institute of Technology Indore, Indore 453552, India*

Accepted XXX. Received YYY; in original form ZZZ

ABSTRACT

The first stars, the chemically pristine Population III, likely played an important role in heating the intergalactic medium during the epoch of cosmic dawn. The very high effective temperatures ($\sim 10^5$ K) predicted for the most massive Population III stars could also give rise to tell-tale signatures in the emission-line spectra of early star clusters or small galaxies dominated by such stars. Important quantities in modelling their observational signatures include their photon production rates at ultraviolet energies at which photons are able to ionize hydrogen and helium, dissociate molecular hydrogen and cause Lyman- α heating.

Here, we model the spectral energy distributions of Population III stars to explore how these key quantities are affected by the initial mass and rotation of Population III stars given a wide range of models for the evolution of these stars. Our results indicate that rotating Population III stars that evolve to effective temperatures $\sim 2 \times 10^5$ K could potentially give rise to a very strong HeII 1640 Å emission line in the spectra from primordial star clusters, without requiring stellar masses of $\gtrsim 100 M_\odot$ indicated by previous models for non-rotating Population III stars. At the same time, the observable impact on 21-cm signatures from cosmic dawn and epoch of reionization from our set of rotating stars that evolve to $\sim 2 \times 10^5$ K are modest, and produce potentially detectable features in the global 21-cm signal and 21-cm power spectrum for high Population III star formation efficiencies only.

Key words: Stars: Population III – stars: rotation – cosmology: dark ages, reionization, first stars – galaxies: high-redshift

1 INTRODUCTION

The first generation of stars, the chemically pristine Population III (hereafter Pop III), is believed to have played an important role in heating the early intergalactic medium during the epoch of cosmic dawn, in producing the first elements beyond lithium, and in the production of early black holes (for a recent review, see [Klessen & Glover 2023](#)). Such stars probably started forming around redshift $z \approx 30$, about 100 Myr after the Big Bang, but may have continued to form in pockets of primordial gas throughout the reionization epoch and well into the post-reionization era (e.g. [Johnson 2010](#); [Mebane et al. 2018](#); [Liu & Bromm 2020](#)). In terms of observational probes, 21-cm cosmology may be able to probe the nature of Pop III stars at $z \approx 15$ –30 through their impact on the temperature state of the intergalactic medium (e.g. [Pochinda et al. 2024](#); [Gessey-Jones et al. 2025](#); [Ventura et al. 2025](#)). At somewhat lower redshifts ($z \approx 6$ –15) one may hope to detect Pop III signatures in individual objects, either among samples of gravitationally lensed, high-redshift stars ([Windhorst et al. 2018](#); [Zackrisson et al. 2024](#)), in gravitationally lensed Pop III star clusters and galaxies ([Zackrisson et al. 2012](#); [Vanzella et al. 2023](#); [Fujimoto](#)

[et al. 2025](#)), or within galaxies where Pop III star formation is able to continue alongside metal-enriched star formation (e.g. [Sarmiento et al. 2018](#); [Venditti et al. 2023](#); [Maiolino et al. 2024](#); [Wang et al. 2024](#)). Other ways of empirically studying the properties of Pop III stars include the chemical signatures of Pop III supernovae in gas absorption systems (e.g. [D’Odorico et al. 2023](#); [Sodini et al. 2024](#); [Vanni et al. 2024](#)), in high-redshift quasars ([Yoshii et al. 2022](#)) and in second-generation stars in the local Universe (e.g. [Fraser et al. 2017](#); [Ishigaki et al. 2018](#); [Jiang et al. 2024](#)), as well as the direct detection of supernovae (e.g. [Moriya et al. 2022](#); [Venditti et al. 2024](#)), gamma-ray bursts (e.g. [Lazar & Bromm 2022](#)), and tidal disruption events ([Kar Chowdhury et al. 2024](#)) produced by Pop III stars.

Due to their chemically pristine composition, Pop III stars are expected to become more massive (e.g. [Klessen & Glover 2023](#)), and reach higher main-sequence temperatures (e.g. [Schaerer 2002](#)) than their metal-enriched descendants. This gives rise to higher hydrogen- and helium-ionizing photon production rates compared to metal-enriched stars, and also differences in the Lyman–Werner (LW; H₂-dissociating) and the Lyman-band rates important for the Wouthuysen–Field coupling during cosmic dawn. However, the production of photons in these different energy regimes depends not only on initial mass but also on stellar rotation (e.g. [Yoon et al. 2012](#);

[★] E-mail: erik.zackrisson@physics.uu.se

Murphy et al. 2021b; Sibony et al. 2022; Liu et al. 2025a,b; Hawcroft et al. 2025), and simulations have indicated that at least some Pop III may rotate at close to break-up speed (Hirano & Bromm 2018).

Here, we use the Muspelheim (Zackrisson et al. 2024) models for the spectral energy distributions (SEDs) of Pop III stars to explore the impact of different sets of stellar evolutionary tracks on the ultraviolet (UV) radiation output of Pop III stars. These models use stellar atmosphere SEDs instead of the blackbody SEDs adopted in many previous studies (e.g. Yoon et al. 2012; Murphy et al. 2021b; Klessen & Glover 2023). In section 2, we present these models and in section 3 we report the resulting hydrogen- and helium-ionizing photon production rates, the LW and the Ly-band rates, along with a comparison to results derived from blackbody SEDs. The impact on studies of the UV SEDs of Population III star clusters and galaxies is explored in Section 4 and the impact on 21 cm-cosmology is shown in Section 5. Various future avenues for improvement of the models are discussed in section 6. Section 7 summarises our findings.

2 SED MODELS OF POPULATION III STARS

The SED models for Pop III stars (Muspelheim v.1.0) presented by Zackrisson et al. (2024) couple sets of stellar evolutionary tracks to a grid of stellar atmospheres to produce SEDs as a function of Zero Age Main Sequence (ZAMS) mass M_{ZAMS} and age. Important simplifications used in the Muspelheim v.1.0 models include the use of stellar atmospheres for spherical stars without mass loss, and with fixed primordial abundances of hydrogen and helium. Hence, these models neglect the non-sphericity that come from high rotation rates, the effects of winds, and the effects of surface helium enhancement and surface self-pollution of metals during the course of evolution. These shortcomings are further discussed in Section 6. In this paper, we make use of Muspelheim SED models based on selected Pop III tracks from Yoon et al. (2012) at $M_{\text{ZAMS}} = 10\text{--}500 M_{\odot}$, Windhorst et al. (2018) at $M_{\text{ZAMS}} = 10\text{--}100 M_{\odot}$, Murphy et al. (2021a) at $M_{\text{ZAMS}} = 1.7\text{--}120 M_{\odot}$, Volpato et al. (2023) at $M_{\text{ZAMS}} = 100\text{--}1000 M_{\odot}$ and Costa et al. (2025) at $M_{\text{ZAMS}} = 6\text{--}200 M_{\odot}$. Out of these sets, the Yoon et al. (2012) and Murphy et al. (2021a) sets feature models both with and without rotation. Although Yoon et al. (2012) present stellar evolutionary tracks for several different initial velocities in the range $0.0\text{--}0.6 v_K$ (where v_K is the Keplerian velocity at the equatorial surface), here we limit the discussion to the $v_K = 0.0$ and 0.4 models, for simplicity.

While many of these tracks are similar close to the ZAMS, they differ significantly in their predictions of their low- T_{eff} extension at late stages of stellar evolution. While Zackrisson et al. (2024) argue that late evolution to $T_{\text{eff}} \lesssim 15000$ K have important consequences for the prospects of detecting lensed, individual Pop III stars at high redshifts, one could expect that such differences would be minor when it comes to the UV photon production rates of Pop III stars, since these are dominated by the more long-lived high- T_{eff} stages of these stars. However, the Yoon et al. (2012) tracks for rotating stars, which also include the effects of magnetic fields, differ from many other models of rotating Pop III stars in the literature (e.g. Murphy et al. 2021a; Sibony et al. 2022; Martinet et al. 2023; Volpato et al. 2024; Tsiatsiou et al. 2024) in that some of the stars with high initial rotation velocity evolve to very high T_{eff} (~ 250000 K) at bolometric luminosities an order of magnitude above their ZAMS luminosities at the end of their lifetimes (similar effects are, however, seen in the rotating Pop III models in the recent paper by Hassan et al. 2025), with significant impact on their UV properties.

In this paper, we explore the UV properties of Pop III stars in terms

of their production of H-, He- and He⁺-ionizing photons, as well as their production of LW and Lyman-band photons. The instantaneous photon production rates Q , expressed in units of photons per second, are defined as:

$$Q_i = \int_{\lambda_1}^{\lambda_2} \frac{\lambda L_{\lambda}}{hc} d\lambda, \quad (1)$$

where L_{λ} is the monochromatic luminosity ($\text{erg}^{-1} \text{s}^{-1} \text{\AA}^{-1}$) at wavelength λ , h is Planck's constant and c the speed of light. The integration limits for the different rates are: $\lambda_1 = 0$ and $\lambda_2 \approx 912 \text{\AA}$ for Q_{H} ; $\lambda_1 = 0$ and $\lambda_2 \approx 504 \text{\AA}$ for Q_{He} ; $\lambda_1 = 0$ and $\lambda_2 \approx 228 \text{\AA}$ for Q_{He^+} ; $\lambda_1 \approx 912 \text{\AA}$ and $\lambda_2 = 1107 \text{\AA}$ for Q_{LW} ; $\lambda_1 \approx 912 \text{\AA}$ and $\lambda_2 = 1216 \text{\AA}$ for Q_{Ly} . We also present $\epsilon_{\text{b}}^{\text{Ly}}$, the Lyman-band photon production count per baryon, integrated over the stellar lifetime t_{lifetime} , given by:

$$\epsilon_{\text{b}}^{\text{Ly}} = \frac{m_{\text{p}}}{M_{\text{ZAMS}}} \int_0^{t_{\text{lifetime}}} Q_{\text{Ly}}(t) dt, \quad (2)$$

where m_{p} is the mass of a proton.

3 IONIZING AND LYMAN-WERNER FLUXES

As previously shown by e.g. Bromm et al. (2001), Larkin et al. (2023), and Liu et al. (2025a), the SEDs of stellar atmosphere models predict UV properties of hot Pop III stars that deviate from those of blackbody SEDs scaled to the same effective temperatures T_{eff} and bolometric luminosities L_{bol} . We illustrate this in Fig. 1, where we compare the SEDs of the TLUSTY stellar atmosphere models used in Muspelheim to those of blackbody SEDs for stars at $T_{\text{eff}} \approx 4 \times 10^4\text{--}2 \times 10^5$ K. The photon counts per wavelength (Q_{λ}) differ between blackbody and stellar atmosphere SEDs in *all* the UV bands, albeit to different extent and in different directions throughout the range of model SEDs shown. It is worth noting, that even though the highest- T_{eff} SED shown ($\approx 2 \times 10^5$ K, a temperature reached only by rotating Yoon et al. (2012) $20\text{--}150 M_{\odot}$ Pop III stars in our set) exhibits the most blackbody-like shape (with small continuum breaks only), the peak of the stellar-atmosphere SED occurs at shorter wavelengths compared to the corresponding blackbody, an effect previously seen in the stellar atmosphere SEDs for Pop III stars by Bromm et al. (2001) and also for pure hydrogen atmospheres for the very hot central stars of planetary nebulae (Rauch 2003).

The effect on the ionizing- and LW photon production rates can be seen in Fig. 2 where we compare results generated from blackbody SEDs (dashed lines; in good agreement with the results presented by Murphy et al. 2021b) and stellar atmospheres (solid lines) for the non-rotating Murphy et al. (2021a) stellar evolutionary tracks with initial masses in the range $9\text{--}120 M_{\odot}$. The general behaviour follows what we would expect from Fig. 1, as the shape¹ of the $T_{\text{eff}} = 4.3 \times 10^4$ K, $T_{\text{eff}} = 5.5 \times 10^4$ K and $T_{\text{eff}} = 9.5 \times 10^4$ K SEDs in Fig. 1 are representative of early evolution along the $9 M_{\odot}$, $15 M_{\odot}$ and $120 M_{\odot}$ Murphy et al. (2021a) tracks in Fig. 2. The blackbody SEDs have consistently higher H-ionizing rates, but lower He-ionizing rates, for all the stellar masses plotted, although by no more than $\approx 0.2\text{--}0.3$ dex. The behaviour of the He⁺-ionizing rates is more complex, as the blackbody under-predicts the flux at $85\text{--}120 M_{\odot}$ by $\approx 0.1\text{--}0.3$ dex, but then severely starts to over-predict the He⁺-ionizing flux by up to ≈ 2 dex at lower masses due to the presence of a strong continuum

¹ But not the L_{bol} scaling, which in Fig. 1 has been chosen to avoid overlap of the SEDs in the plot

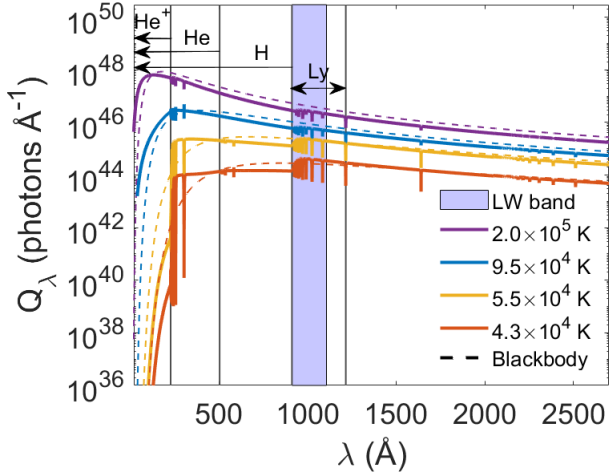


Figure 1. SEDs (in units of photon production rate per unit wavelength) of TLUSTY stellar atmosphere models with primordial chemical composition for $T_{\text{eff}} = 2.05 \times 10^5$ K (purple solid line), $T_{\text{eff}} = 9.5 \times 10^4$ K (blue solid line), $T_{\text{eff}} = 5.5 \times 10^4$ K (yellow solid line) and $T_{\text{eff}} = 4.3 \times 10^4$ K (red solid line), contrasted to the corresponding blackbody SEDs (purple, blue, yellow and red dashed lines). To avoid overlap, the SEDs are scaled to bolometric luminosities $\log(L_{\text{bol}}/L_{\odot}) \approx 6.8, 5.3, 4.3$ and 3.3 , respectively. The surface gravities of the TLUSTY SEDs has been set to $\log(g) = 6.5$ for the $T_{\text{eff}} = 2.05 \times 10^5$ K model and 5.0 in the other cases. The coloured patch indicates the extent of the LW band and the arrows the extent of the Lyman band and the H-, He-, He⁺-ionizing part of the SEDs. Differences between the stellar atmosphere SEDs and the blackbody SEDs are seen in all of the different bands, although the degree to which blackbody models over- or underpredict the rates depend on T_{eff} . The $T_{\text{eff}} = 4.3 \times 10^4$, 5.5×10^4 and 9.5×10^4 K SEDs are considered representative of early evolution along the $9 M_{\odot}$, $15 M_{\odot}$ and $120 M_{\odot}$ Murphy et al. (2021a) Pop III tracks for both rotating and non-rotating stars, whereas the $\approx 2 \times 10^5$ K model is representative only for rotating Yoon et al. (2012) $20\text{--}150 M_{\odot}$ stars at the very end of their lifetimes.

break in the stellar atmosphere SEDs at the He⁺ edge (seen in the $T_{\text{eff}} = 5.5 \times 10^4$ K and 4.3×10^4 K SEDs in Fig. 1). In the case of the LW flux, the blackbody SED over-predicts the flux by up to ≈ 0.15 dex at the highest masses (as seen in the $T_{\text{eff}} = 9.5 \times 10^4$ K SED), becomes nearly identical at $15 M_{\odot}$ (as seen in the $T_{\text{eff}} = 5.3 \times 10^4$ K SED) and drops below the stellar atmosphere SED by ≈ 0.1 dex by $9 M_{\odot}$ (as seen in the $T_{\text{eff}} = 4.3 \times 10^4$ K SED).

When modelling the impact of Pop III stars on the intergalactic medium, the detailed temporal evolution of the UV photon rates is often neglected in favour of lifetime-integrated quantities (for a counterexample, see Gessey-Jones et al. 2022). This may be reasonable in cases where the lifetimes of the Pop III stars are short compared to timescales related to the thermal evolution of the IGM or changes in cosmic star formation rate density, as is the case for the more massive Pop III stars. In Fig. 3 we present the lifetime-integrated photon production rates of our Pop III models per solar mass, compared to blackbody models from Klessen & Glover (2023) and models for rotating stars with homogeneous chemical evolution from Liu et al. (2025a, further discussed in section 5). For stellar masses $M \gtrsim 10 M_{\odot}$, all models except the Yoon et al. (2012) and Liu et al. (2025a) rotating models agree on the H-ionizing and He-ionizing rates to within ≈ 0.3 dex. The Yoon et al. (2012) models at $20 \lesssim M_{\text{ZAMS}} \lesssim 200 M_{\odot}$, and all of the Liu et al. (2025a) models, undergo chemically homogeneous evolution which significantly boosts the ionizing photon production of these stars. At lower masses,

models based on blackbodies are seen to deviate from those based on stellar atmosphere SEDs by up to ≈ 3 dex for H and ≈ 5 dex for He.

In the case of the He⁺-ionizing photon production rates, models based on blackbody SEDs at $M \lesssim 100 M_{\odot}$ consistently produce higher values than corresponding models based on stellar atmosphere SEDs, as expected from Fig. 2, with an offset that reaches ≈ 6 dex at the lowest masses. Models for rotating Yoon et al. (2012) stars at $20\text{--}300 M_{\odot}$ produce higher He⁺-ionizing rates than all other models at comparable masses. This increase of He⁺-ionizing photons due to rotation was already highlighted by Yoon et al. (2012), although the increase compared to non-rotating models becomes much higher in models based on stellar atmosphere SEDs (peaking at ≈ 3.8 dex at $20 M_{\odot}$) compared to the blackbody SEDs ($\lesssim 1.4$ dex) used by Yoon et al. (2012), as shown in their fig. 7. Liu et al. (2025a) is not included in the He⁺ panel as their spectra are cut off at 124 \AA which leaves out a significant portion of the He⁺-ionizing photons, especially at high T_{eff} (Fig. 1).

For the LW band, models that undergo CHE produce somewhat lower rates ($\approx 0.2\text{--}0.3$ dex) than other models at $\gtrsim 50 M_{\odot}$ while lower masses produce rates on the higher side compared with other models. The Klessen & Glover (2023) blackbody models also produce systematically lower rates at low stellar masses (reaching offsets of ≈ 0.85 dex at $1.7 M_{\odot}$) compared to models based on stellar atmosphere SEDs. At high masses, the most notable outliers are the models by Schaerer (2002), which at $M > 5 M_{\odot}$ produce much higher rates than all other models (up to ≈ 0.7 dex higher). This discrepancy is discussed further in Section 6.2.

The lifetime-average photon production rates corresponding to the lifetime-integrated rates in Fig. 3 for our Yoon et al. (2012) and Murphy et al. (2021a) models can be found in Table A1. $Q(t)$ tables and both lifetime-integrated and lifetime-average photon production rates for all models can be downloaded from the Muspelheim webpage (see Section 7).

4 IMPACT ON THE THE HEII λ 1640 EMISSION LINE FROM POPULATION III STAR CLUSTERS

The very high He⁺-ionizing photon production rates of Pop III rotating Yoon et al. (2012) stars are interesting in the context of HeII emission lines from high-redshift galaxies. In particular, the HeII λ 1640 emission line has been proposed as a potential Pop III signature, as it can become very strong (with rest-frame equivalent widths up to $\text{EW}_{1640} \sim 100 \text{ \AA}$) in the presence of $T_{\text{eff}} \sim 10^5$ K stars (e.g. Tumlinson & Shull 2000; Schaerer 2002; Raiter et al. 2010; Nakajima & Maiolino 2022). For non-rotating stars, effective temperatures required to produce $\text{EW}_{1640} \gtrsim 30 \text{ \AA}$ are not reached until $\sim 100 M_{\odot}$, which means that a very strong HeII λ 1640 line from an integrated stellar population (Pop III star cluster or Pop III-dominated galaxy) could serve as an indicator of a top-heavy Pop III stellar initial mass function. Recently, a system with $\text{EW}_{1640} \gtrsim 30 \text{ \AA}$ and no detectable metal lines, located in the halo of the galaxy GNz-11 at $z \approx 10.6$, was found by Maiolino et al. (2024) who interpreted this as evidence of a Pop III IMF extending at least up to $500 M_{\odot}$.

In Fig. 4, we explore the temporal evolution of the He⁺-ionizing rates of our Yoon et al. (2012) models, with and without rotation. Since rotation in these models shifts the early main sequence to lower T_{eff} and slightly lower bolometric luminosities, rotation leads to lower He⁺ rates during early evolution (although this phase is very brief in the case of the $500 M_{\odot}$ model). However, since the rotating stars eventually evolve to become hotter and more luminous than their

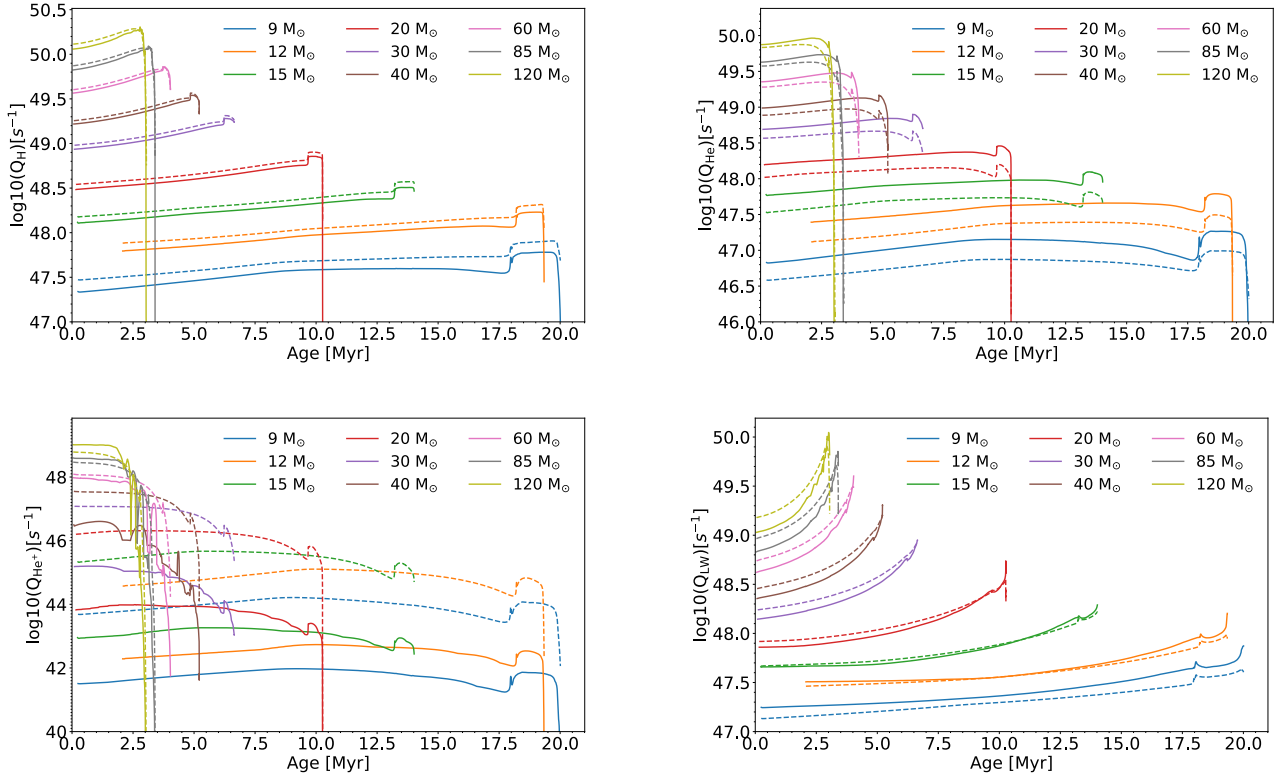


Figure 2. Photon productions rates (Q_i) as a function of stellar age for [Murphy et al. \(2021b\)](#) non-rotating models. The top left panel is for H-ionizing photons, the top right He-ionizing, the bottom left He^+ -ionizing, and the bottom right LW-photons. Solid lines represent predictions based on stellar atmospheres and dashed lines the corresponding predictions for black body spectra. The largest difference between photon production rates of black body and atmospheres is the over-prediction of He^+ -ionizing photons for black bodies, reaching up to ~ 2.3 dex for the less massive stars. As expected from Fig. 1, the effect becomes smaller for the higher-mass stars and even inverses for the most massive, as a result of their high T_{eff} ($\approx 9.5 \times 10^4$ K for the $120 M_{\odot}$ model) close to the ZAMS. The other photon production rates are less drastically affected.

non-rotating counterparts for $M > 10 M_{\odot}$, the He^+ -ionizing photon rates of these rotating stars grow by several orders of magnitude at high ages. This effect, coupled to the extended lifetimes of these stars (due to rotational mixing renewing the fuel in the core), explains the boosted time-integrated Q_{He^+} rates for rotating [Yoon et al. \(2012\)](#) models shown in Fig. 3.

Since Fig. 4 indicates that the He^+ -ionizing rates of these 20–30 M_{\odot} rotating models can become comparable, for about ~ 1 Myr at the end of their lifetimes, to the peak He^+ -ionizing rates of 100–150 M_{\odot} stars (maintained over a similar timescale, but during early evolution), it seems that very strong $\text{HeII}\lambda 1640$ emission in principle could be produced by rotating Pop III stars without the presence of $M \gtrsim 100 M_{\odot}$ stars.

To explore this, we use the latest version of the photoionization code CLOUDY (v23.01), last described by [Chatzikos et al. \(2023\)](#) and [Gunasekera et al. \(2023\)](#) to investigate the effect of gas parameters on the line strength and equivalent width of the $\text{HeII}\lambda 1640$ emission line in gas clouds surrounding single stars from the [Yoon et al. \(2012\)](#) set. We assume primordial gas abundances, a plane-parallel nebula, and an ionization parameter in the range $U = -1$ to -4 .

In Fig. 5 we show the resulting equivalent widths of the $\text{HeII}\lambda 1640$ emission line for a subset of [Yoon et al. \(2012\)](#) tracks. Comparing our results with $\text{HeII}\lambda 1640$ EWs from [Schaerer \(2003\)](#) and [Raiter et al. \(2010\)](#) – which both assume fully sampled Pop III IMFs – we are able to obtain only slightly higher $\text{HeII}\lambda 1640$ equivalent widths than the most extreme values seen in their models. However, the major

difference is that both [Schaerer \(2003\)](#) and [Raiter et al. \(2010\)](#) require IMFs dominated by very massive stars to reach the high EWs that we are able to obtain for 20 M_{\odot} stars. We also explore other ionization parameters, not shown in the figure, and find that the equivalent widths are largely stable at $\log(U) \geq -3$, but note a significant drop at $\log(U) = -4$ in agreement with [Raiter et al. \(2010\)](#).

Our results indicate that a stellar population of [Yoon et al. \(2012\)](#) rotating stars with an IMF peaking at $\sim 20 M_{\odot}$ in principle could produce equally strong $\text{HeII}\lambda 1640$ equivalent widths as what has been seen for Pop III models with non-rotating stars and more top-heavy IMFs (like the 50–500, Salpeter-slope, and the $M_c = 60, \sigma = 1, 1\text{--}500 M_{\odot}$ lognormal model from [Raiter et al. 2010](#)). However, it is important to note that since the $T_{\text{eff}} \sim 10^5$ K phase of the 20 M_{\odot} rotating [Yoon et al. \(2012\)](#) model is reached only at the very end of its ≈ 15 Myr lifetime, a Pop III system that also hosts more massive stars (with lifetimes as short as ≈ 2 Myr for the models considered here) may already have exploded as supernovae and cleared away any remaining gas from the vicinity of the stars, which would lead to very low ionization parameters and reduced $\text{HeII}\lambda 1640$ equivalent widths. In the case of low-mass haloes and sufficiently powerful supernovae, the gas may even be completely removed from the halo, which would preclude the detection of any emission lines associated with the late evolution of these 20 M_{\odot} stars. Even without supernovae, the initially dense gas around a cluster of Pop III stars in $\lesssim 10^8 M_{\odot}$ haloes may be expelled to large radii and low densities in response to the radiation field from the stars, with long recombination time-scales

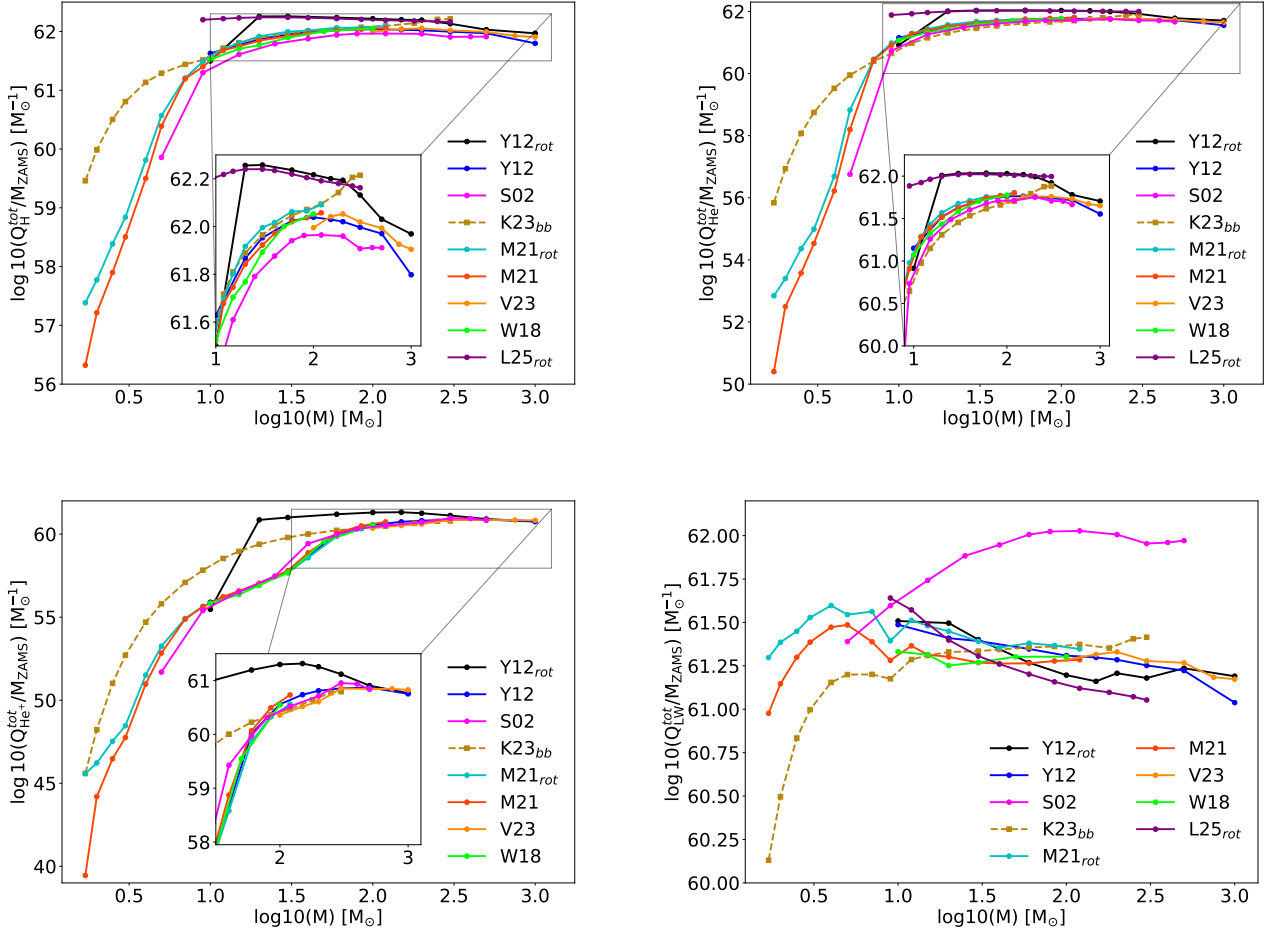


Figure 3. Lifetime-integrated UV photon productions rates per solar mass from rotating and non-rotating models with tracks from Yoon et al. (2012, black and blue; Y12_{rot} and Y12), Murphy et al. (2021b, teal and red; M21_{rot} and M21), Volpato et al. (2023, yellow; V23), Windhorst et al. (2018, green; W18), Klessen & Glover (2023, maroon; K23_{bb}), Schaerer (2002, magenta; S02), and Liu et al. (2025a, purple; L25_{rot}). The top left gives the values for H-ionizing photons, the top right for He-ionizing, the bottom left for He⁺-ionizing, and the bottom right for LW photons. The values from Klessen & Glover (2023) are based on tracks from Murphy et al. (2021b) and Martinet et al. (2023), using black body spectra which is why they differ from the other models, especially at lower masses. Liu et al. (2025a) is omitted from the He⁺ panel as they only include wavelengths above 124Å. In general, all models based on stellar atmosphere SEDs agree on the H-ionizing and He-ionizing fluxes to within ≈ 0.3 dex for non-rotating stars at $M \gtrsim 10 M_{\odot}$ and within ≈ 0.7 dex when rotation is included for these masses. The use of black body spectra severely overpredicts the He⁺-ionizing fluxes compared to comparable models based on stellar atmosphere SEDs. However, models for rotating Yoon et al. (2012) stars at 20–300 M_{\odot} produce higher He⁺-ionizing fluxes than all other models. In the LW-band, the Schaerer (2002) predictions constitute a significant outlier which we discuss further in section 6.2.

and significant leakage of ionizing photons into the intergalactic medium as a result (e.g. Sibony et al. 2022). Detailed simulations would be required to assess whether rotating 20 M_{\odot} stars would realistically be able to produce strong HeII emission lines (at the level of the recently detected Maiolino et al. 2024 Pop III galaxy candidate) late in the lifetimes of these stars, even if evolution were to follow the Yoon et al. (2012) models.

5 IMPACT ON THE 21 CM SIGNAL FROM COSMIC DAWN

The impact of Pop III stars on the cosmic 21-cm signal is multifold. During the epoch of cosmic dawn, the Lyman-band continuum flux of Pop III stars plays an important role through the Wouthuysen–Field (WF) effect, wherein Lyman- α photons scatter off neutral hydrogen in the intergalactic medium and act to couple the 21-cm spin

temperature to the kinetic temperature of the gas. The scattering of Lyman-line photons also acts to raise the kinetic temperature of the intergalactic medium. At the same time, LW photons dissociate H₂ molecules, suppressing further Pop III star formation in molecular cooling dark matter minihaloes. During the epoch of reionization, Pop III stars that are still able to form ionize their surrounding gas, leading to a suppression in the 21-cm signal.

In Fig. 6, we plot the lifetime-integrated Lyman-band photon production rates per ZAMS stellar baryon ϵ_b^{Ly} of our Pop III models in relation to the corresponding predictions presented by Gessey-Jones et al. (2022) for non-rotating Pop III stars, and those of Liu et al. (2025a) for rotating Pop III stars. Both of these are, like the Muspelheim ones, based on TLUSTY stellar atmosphere SEDs, but employ different assumptions concerning stellar evolution. The Gessey-Jones et al. (2022) and Liu et al. (2025a) models both trace evolution up to the end of main sequence under the assumption of no mass loss,

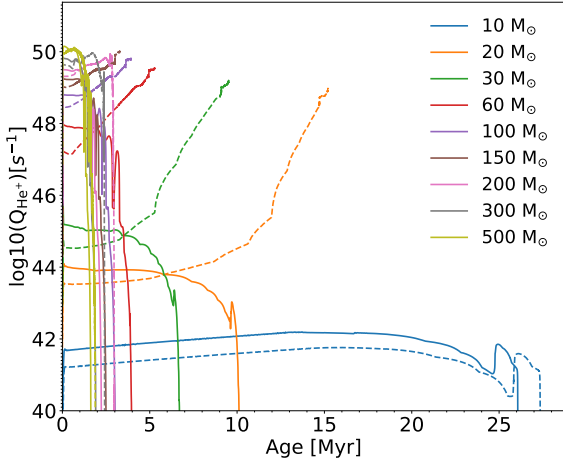


Figure 4. Comparison of He^+ ionizing fluxes of rotating and non-rotating tracks from Yoon et al. (2012). The dashed lines show rotating models with initial velocity $v = 0.4v_k$ and the solid lines show the corresponding non-rotating models. Large differences between rotating and non-rotating stars are seen for $> 10 M_\odot$ due to extended lifetimes for rotating stars and the very high temperatures ($\approx 2 \times 10^5$ K) that 20–150 M_\odot rotating stars evolve to at the end of their lifetimes.

whereas our models also include later evolutionary stages and – in the case of Yoon et al. (2012) models with rotation – substantial mass loss. Whereas the Gessey-Jones et al. (2022) models are based on non-rotating stars, the Liu et al. (2025a) models are based on Sibony et al. (2022) tracks for polytrope stars subject to chemically homogeneous evolution due to strong internal mixing. While Sibony et al. (2022) choose to remain agnostic about the physical reason for what would cause this mixing, fast rotation represents a strong candidate, as evident by the rotating Yoon et al. (2012) models, which in many cases also undergo chemically homogeneous evolution. For simplicity, we hereafter refer to the Liu et al. (2025a) models as rotating, in line with the discussion of these models by Liu et al. (2025a,b).

Differences in ϵ_b^{Ly} between the models at any given mass are within about a factor of two, with the rotating stars below 30 M_\odot consistently resulting in higher rates compared with their non-rotating counterparts due to their increased lifetimes. Interestingly for our discussion, we note a large difference compared to the Gessey-Jones et al. (2022) models at a mass of 20 M_\odot , where the Yoon et al. (2012) models for rotating stars (which have the potential to boost the HeII λ 1640 emission line equivalent width; Fig. 5) give rise to an ϵ_b^{Ly} that is higher by a factor of ≈ 1.7 . Since it is important to establish whether differences of this amplitude could have any significant impact on 21-cm signatures from the pre-reionization Universe, we use the semi-numerical code 21cmSPACE (e.g. Fialkov et al. 2014; Reis et al. 2021; Gessey-Jones et al. 2022, 2025)² to simulate the global 21-cm signal and the spherically averaged 21-cm power-spectrum $\Delta_{21}(k, z)$ at $z = 6\text{--}40$, under the extreme assumption of a single-star initial mass function where all Pop III stars have the same mass (a rough approximation of the case where the initial mass function is strongly peaked at this mass).

The simulations are performed on cosmological box size of

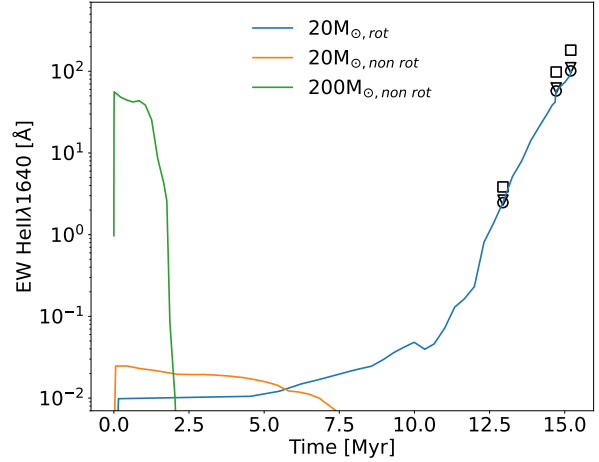


Figure 5. Equivalent widths of the HeII λ 1640 line as a function of time for the Yoon et al. (2012) 20 M_\odot rotating and non-rotating stars, with the non-rotating 200 M_\odot star included for comparison. The parameters used in the CLOUDY calculations are $\log U = -2$ and $n(\text{H}) = 10^2$. At three points we show the equivalent widths for hydrogen density $n(\text{H}) = 10^1$ (circles), 10^3 (triangles), and 10^4 (squares). The 20 M_\odot star reaches equivalent widths surpassing the maximum of the 200 M_\odot star at the end of its lifetime. Increasing the hydrogen density in the nebular cloud is seen to slightly increase the equivalent width.

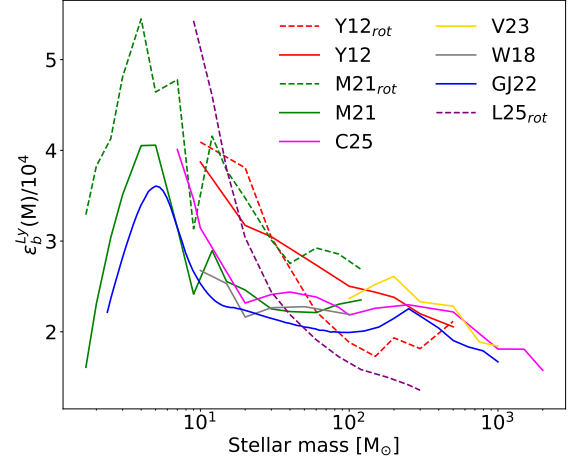


Figure 6. Total Lyman-band emission per stellar baryon as a function of ZAMS mass for the various stellar models considered in this work. Results from Gessey-Jones et al. (2022, GJ22) are shown in blue for comparison (cf. their fig. 5). The rotating models from Murphy et al. (2021a, M21_{rot}) exhibit a clear enhancement in Lyman-band emission, primarily due to their extended lifetimes. In contrast, the Yoon et al. (2012, Y12_{rot} and Y12) and Liu et al. (2025a, L25_{rot}) models display a more nuanced behaviour: while rotating stars with $M_{\text{ZAMS}} \lesssim 60 M_\odot$ emit more than their non-rotating counterparts from other studies, their emission falls below that of non-rotating Yoon et al. (2012) models for $M_{\text{ZAMS}} \gtrsim 30 M_\odot$ and $\gtrsim 20 M_\odot$ respectively.

² <https://www.cosmicdawnlab.com/21cmSPACE>

(384 cMpc)³, and include effects such as baryon dark-matter streaming velocity, Lyman- α heating and scattering and Lyman-Werner feedback (important during the cosmic dawn) as well as photoheating feedback, X-ray heating and ionization from flexible spectra models (important during the epoch of reionization). In particular, for this work, we use the code version described in Liu et al. (2025a) where the effect of ionizing photons from Pop III stars was introduced. To put the Yoon et al. (2012) Pop III models into context, we also run 21cmSPACE with the Pop III models of Gessey-Jones et al. (2022) and Liu et al. (2025a).

We consider two sets of astrophysical parameters for comparison:

Scenario 1: $f_{\star, \text{II}} = 5\%$, $f_{\star, \text{III}} = 0.2\%$, $t_{\text{rec}} = 30\text{Myr}$

Scenario 2: $f_{\star, \text{II}} = 1\%$, $f_{\star, \text{III}} = 0.5\%$, $t_{\text{rec}} = 100\text{Myr}$

where $f_{\star, \text{II}}$ and $f_{\star, \text{III}}$ represent the star formation efficiency for Pop II and III stars, respectively, and t_{rec} is the recovery time for star formation after the onset of Pop III supernovae. Due to the higher $f_{\star, \text{III}}/f_{\star, \text{II}}$ ratio and the longer t_{rec} of scenario 2, the impact of the detailed properties of Pop III stars on 21 cm observables during cosmic dawn will be higher for this model compared to that of scenario 1. To pinpoint the role of Lyman-band emissivities of Pop III stars in shaping the 21-cm signal, we switch off X-ray heating from Pop III stars. For Pop II, we adopt an X-ray luminosity L_X tied to the star formation rate (SFR) of each halo, according to $L_X/\text{SFR} = 3 \times 10^{40} \text{ erg s}^{-1} \text{ M}_{\odot}^{-1} \text{ yr}^{-1}$ (Fragos et al. 2013a,b). Throughout, we assume instantaneous emission from Pop III stars, which is a reasonable assumption for stellar masses $\gtrsim 10 \text{ M}_{\odot}$ (Gessey-Jones et al. 2022).

Fig. 7 shows the resulting global 21-cm signal, and the power spectrum generated at a scale of $k = 0.24 \text{ cMpc}^{-1}$, for the Yoon et al. (2012) 20 M_{\odot} model with rotation, in comparison with the 20 M_{\odot} model from Gessey-Jones et al. (2022) without rotation, the 20 M_{\odot} from Liu et al. (2025a) with rotation, and the 20 and 200 M_{\odot} Yoon et al. (2012) model without rotation. The 200 M_{\odot} model is included here as an example of a type of star that, because of its high T_{eff} , could produce strong HeII $\lambda 1640$ emission despite being non-rotating (Fig. 5).

In the case of the 21-cm power spectra, we also plot the expected 5σ detection limit for 1080 hours of tracking-scan observations using the Square Kilometre Array (SKA-Low) with 6 hours of observation per night for 180 days. The derived detection limit considers both the thermal noise and the sample variance. To estimate the uncertainty in the power spectrum due to thermal noise, we used the package 21cmSense³ (Pober et al. 2013, 2014). We only considered the SKA-Low AA* array configuration (Sridhar et al. 2024) within a radius of 2 km from the array center and assumed the moderate foreground model in 21cmSense. The sample variance is calculated according to the equation

$$\sigma_{\text{sample}}^2 = \frac{\sum n_i (k_i - \bar{k})^2}{N - 1}, \quad (3)$$

where N is the total number of counts and n_i is the number of counts in the k_i -bin. The total noise is then estimated as the sum of thermal noise and sample variance in quadrature:

$$\sigma_{\text{total}} = \sqrt{\sigma_{\text{sample}}^2 + \sigma_{\text{thermal}}^2}. \quad (4)$$

5.1 The global 21-cm signal

The differences in the global signal between the Pop III stellar models can be explained by considering the epochs $z \sim 25$ where the early onset of the global signal absorption trough is almost entirely dictated by the Lyman band emissivities (Fig. 6)⁴, while the absorption trough at $z \sim 15$ is also sensitive to the ionizing flux from the stars (Fig. 3).

During the cosmic dawn ($z \approx 20 - 30$), a higher Lyman-band flux $\epsilon_{\text{b}}^{\text{Ly}}$ leads to a stronger WF effect and more rapid onset of significant 21-cm absorption. This would be strongest for the rotating 20 M_{\odot} Yoon et al. (2012) model and weakest for the non-rotating 20 M_{\odot} Gessey-Jones et al. (2022) and non-rotating 200 M_{\odot} Yoon et al. (2012) model. Since the latter two exhibit similar Lyman fluxes, they have nearly identical global signal absorption amplitude at $z \gtrsim 20$ in both scenarios 1 and 2. The rotating 20 M_{\odot} Liu et al. (2025a) model and non-rotating 20 M_{\odot} Yoon et al. (2012) model fall in between these extremes and approximately similar behaviour. The difference in the 21-cm signal at these high redshifts ($z \approx 20 - 30$) is of the order of few mK in scenario 1 and up to 20 mK at its largest in scenario 2.

During the epoch of heating and reionization ($z \lesssim 20$), the differences in these models is dominated by the ionization from Pop III stars (as explored in Liu et al. 2025a). In this case, the rotating 20 M_{\odot} stellar models from Yoon et al. (2012) and Liu et al. (2025a) predict similarly strong ionizing fluxes which manifest as weak emission signal at $z \lesssim 10$ for scenario 1, and a suppressed absorption trough at $z \approx 15$ for scenario 2. Indeed, with these more extreme stellar models, there is already a 10–20 per cent reduction in the neutral hydrogen fraction at $z \approx 15$ (see Fig. A1), and a proportional suppression of the signal. This is also true for the case of the non-rotating 200 M_{\odot} Yoon et al. (2012) model, while the 20 M_{\odot} non-rotating models of Yoon et al. (2012) and Gessey-Jones et al. (2022) produce deeper troughs due to late reionization.

5.2 The 21-cm power spectrum

The predicted high-redshift 21-cm power spectra at $z \gtrsim 20$, for both scenarios 1 and 2, fall below the 5σ detection limit of the SKA. At lower redshifts, where the power spectrum is deemed detectable according to our error model, the differences between models are marginal in scenario 1. Still, they are more pronounced and potentially detectable in scenario 2. The largest difference comes from the ionization signature of rotating Pop III stars. The 20 M_{\odot} Yoon et al. (2012) and Liu et al. (2025a) models, which both undergo chemically homogenous evolution, produce power spectra which deviate from those predicted for the non-rotating 20 M_{\odot} models of Gessey-Jones et al. (2022) and Yoon et al. (2012). In both cases, the emission signal vanishes as the Universe is rapidly ionized, and the ionized bubbles imprint detectable fluctuations in the power spectrum at $z \approx 12.5$. Here too, the non-rotating 200 M_{\odot} Yoon et al. (2012) model shows an intermediate behaviour between the two cases.

Overall, we conclude that the dramatic difference seen between the He⁺-ionizing rates (Fig. 4) and HeII $\lambda 1640$ equivalent widths (Fig. 5) of rotating vs. non-rotating stars do not necessarily translate into equally dramatic 21-cm signatures. While differences due to rotation may be imprinted in the 21-cm power spectrum detectable by SKA, these are only conspicuous in some parts of the Pop III parameter space (i.e. in our scenario 2 where it boosts the ionization peak by factor of a 2–3, but not in scenario 1).

³ <https://github.com/rasg-affiliates/21cmSense/tree/main>

⁴ Although Lyman-Werner photons do contribute to suppression of star-formation in molecular cooling haloes, and we account for this.

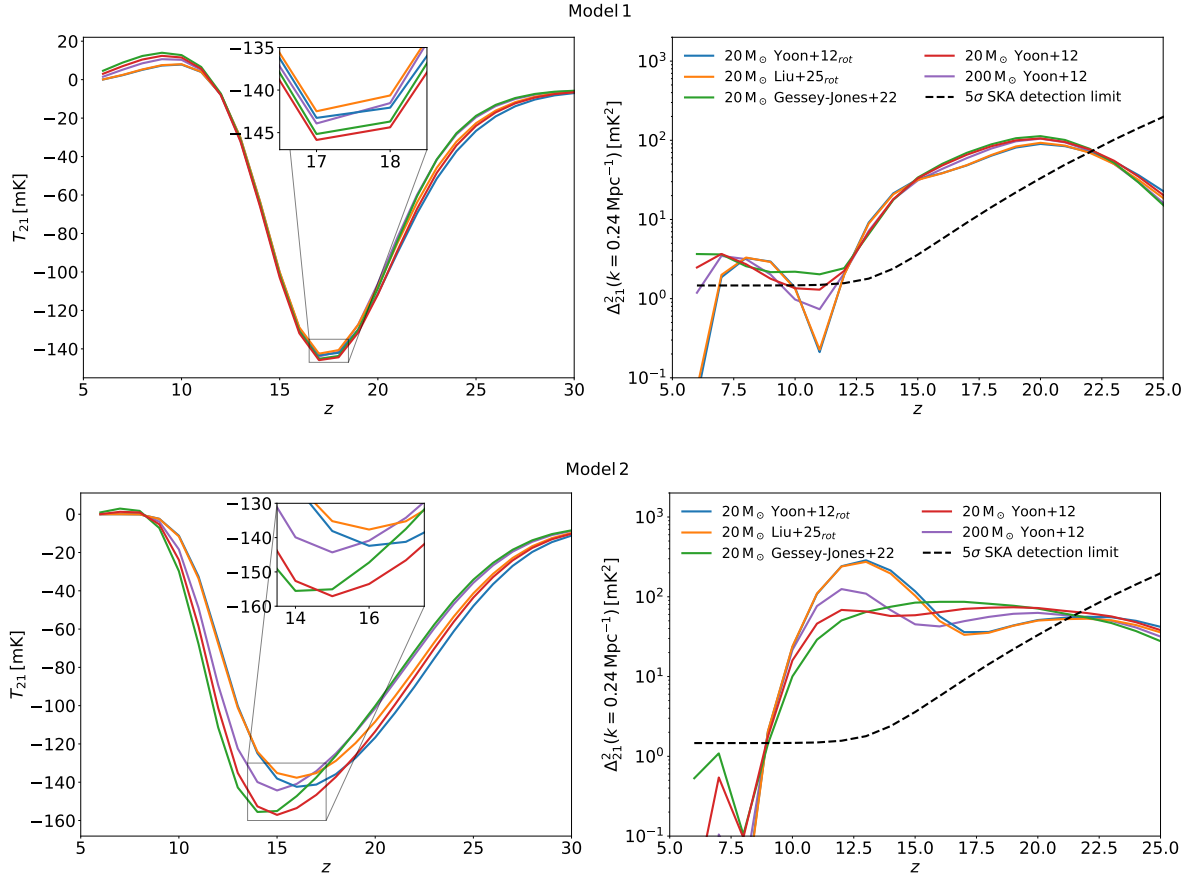


Figure 7. Simulated 21-cm global signal and power spectrum at $k = 0.24 \text{ cMpc}^{-1}$, based on single-mass IMFs for a sample of stars from [Yoon et al. \(2012\)](#), [Gessey-Jones et al. \(2022\)](#), and [Liu et al. \(2025a\)](#). The black line shows the estimated 5σ SKA detection limit from a 1080h observation using the array assembly AA* configuration of SKA1-Low within a radius of 2 km from the array center. Differences between the different models are very small for both the global 21-cm signal and the 21-cm power spectrum in scenario 1, but observationally significant in scenario 2. In scenario 2, the 21-cm signatures of the $20 M_{\odot}$ [Yoon et al. \(2012\)](#) rotating model (capable of producing very strong HeII λ 1640 emission) deviates from those of the $200 M_{\odot}$ [Yoon et al. \(2012\)](#) non-rotating model (also able to produce strong HeII λ 1640 emission), which indicates that 21-cm observations may be able to help break degeneracies between such models.

6 DISCUSSION

6.1 Blackbody versus stellar atmosphere SEDs

When comparing our results with the models presented by [Klessen & Glover \(2023\)](#), based on blackbody spectra, we find in Fig. 3 the largest discrepancy in He^+ ionizing rates for stars $< 100 M_{\odot}$, where blackbody spectra result in rates orders of magnitude higher. These differences, also echoed in our [Murphy et al. \(2021a\)](#) comparison of momentary Q_{He^+} for stellar atmosphere spectra versus blackbody spectra in Fig. 2, are due to the different shapes of blackbody and stellar atmosphere SEDs and the lack of continuum breaks in the former case, as shown in Fig. 1. Hence, blackbody spectra should not be used to estimate Pop III photon production rates or fluxes at such high energies.

We also note a significant deviation in all UV bands for stars $< 9 M_{\odot}$ when comparing blackbody and stellar atmospheres, as shown in Fig. 3. While [Murphy et al. \(2021b\)](#) did comment on the reliability of the blackbody approximation for the [Murphy et al. \(2021b\)](#) tracks (through a comparison to the results of [Schaerer 2002](#)), this offset was not noted since the [Murphy et al. \(2021b\)](#) study of UV photon production rates considered only stars of masses $\geq 9 M_{\odot}$ from the [Murphy et al. \(2021a\)](#) set. The blackbody approximation from their

lower-mass tracks is adopted by [Klessen & Glover \(2023\)](#) which overestimate the ionizing rates for all low mass stars and slightly underestimate the LW rates for these same stars. However, as long as the Pop III IMF is assumed to be top-heavy, this discrepancy should not be a major source of error, as the ionizing photon production in that case would be dominated by the more massive stars.

6.2 The Lyman–Werner emissivities of Pop III stars

The LW photon production rates of Pop III stars are important for establishing the LW radiation background during cosmic dawn and for the quenching of subsequent star formation in low-mass haloes. When the lifetime-integrated Q_{LW} is expressed as LW photons per stellar baryon, there are two distinct values that are frequently featured in the literature: 4800 and $\sim 10^5$. Our models do not favour either of these, but instead favour values in the intermediate range $\approx 8 \times 10^3$ to 3×10^4 (see Fig. 3; $\log Q_{\text{LW}}/M_{\text{ZAMS}}$ values in this figure can be converted to log LW photons per stellar baryon by subtracting ≈ 57.08). The lower literature value (4800) stems from [Barkana & Loeb \(2005\)](#), based on Pop III spectra from [Bromm et al. \(2001\)](#) and an adopted power-law slope of the spectrum, whereas the higher value ($\sim 10^5$) is usually attributed to [Schaerer \(2002\)](#). Indeed, when

the [Schaerer \(2002\)](#) Table 4 values are converted into these units, they peak at $\sim 9 \times 10^4$ LW photons per baryon at a Pop III stellar mass of $60 M_{\odot}$. However, as shown in Fig. 3, the [Schaerer \(2002\)](#) Q_{LW} are higher than ours at $M \gtrsim 10 M_{\odot}$ by up to a factor ≈ 5 (0.7 dex). [Mas-Ribas et al. \(2016\)](#) also note difficulties in reproducing the [Schaerer \(2002\)](#) LW rates and suggest that the [Schaerer \(2002\)](#) LW rates may have been integrated from 11.2 eV (wavelength 1107 Å) to infinity, rather than to 13.6 eV (wavelength 912 Å), which would lead to boosted rates. Lifetime-integrated LW rates per stellar baryons in the $\sim 10^5$ range for Pop III stars are also reported in the recent paper by [Costa et al. \(2025\)](#), and in that case the LW rates were indeed integrated from 11.2 eV to infinity (Guglielmo Costa, private communication). After correcting the [Costa et al. \(2025\)](#) limit from 11.2 to 13.6 eV, their values agree with ours. Our values are moreover in good agreement with those recently presented by [Liu et al. \(2025a\)](#) for the non-rotating Pop III tracks of [Gessey-Jones et al. \(2022\)](#) and the rotating Pop III tracks of [Sibony et al. \(2022\)](#). Hence, our recommendation is to use values for the lifetime-integrated LW photon counts per stellar baryons of $\approx 8 \times 10^3$ to 3×10^4 .

6.3 Viability of the stellar atmosphere models

The results in this paper are based on SED models for Pop III stars, which at $T_{\text{eff}} > 15000$ K make use of TLUSTY ([Hubeny & Lanz 1995](#)) stellar atmosphere models for plane-parallel, hydrostatic stars with primordial surface composition. While certainly more realistic than blackbody SEDs, such stellar atmosphere models may still represent an oversimplification that could impact the emitted ionizing photon production rates of Pop III stars. The surface He/H composition of Pop III stars may change over the course of their lifetimes, and the surface may also get polluted by metals produced within the star, due to either chemically homogeneous evolution for a rapidly rotating star (e.g. [Yoon et al. 2012](#); [Liu et al. 2025a](#)), but also due to dredge-ups for a non-rotating star (e.g. [Volpato et al. 2023](#)).

While [Schaerer \(2002\)](#) notes that the impact of the H/He level on the stellar atmosphere spectra is small, this statement likely does not apply to models for rotating stars with helium mass fractions close to unity ([Sibony et al. 2022](#)). [Liu et al. \(2025a\)](#) do take the evolving helium abundance into account in their modelling of Pop III stars, and while they note that this helps the stellar atmosphere model converge, no analysis of the impact of the pure-helium atmosphere on the emerging stellar atmosphere spectra was presented in their paper.

Indeed, as shown in [Zackrisson et al. \(2024\)](#), the set of TLUSTY stellar atmosphere models used by Muspelheim (with fixed H/He fractions) are – due to convergence problems – sometimes unable to reach the low surface gravities of all Pop III stellar evolutionary tracks. This is for instance the case of the $T_{\text{eff}} \sim 2 \times 10^5$ K state of $20 M_{\odot}$ [Yoon et al. \(2012\)](#) stars with rotation highlighted in Section 4 in relation to its potential to produce a very strong HeII λ 1640 emission line. These $20 M_{\odot}$ rotating stars lie $\Delta \log(g) \approx 0.25$ below the last converged grid data point. However, judging by how the He^+ -flux changes with $\log(g)$ within the converged grid at these T_{eff} , this is likely to have a very minor effect on Q_{He^+} .

Rotational mixing and surface composition can also be affected by the presence of a companion Pop III star in a binary system ([Song et al. 2020](#)). Rapid rotation could furthermore drive a mechanical wind, and metals at the surface of Pop III stars may also trigger line-driven winds (e.g. [Liu et al. 2021](#); [Jeena et al. 2023](#)). The effects of winds on the emerging ionizing photon production rates of Pop III stars were explored by [Schaerer \(2002\)](#), who concluded that the ionizing photon rates would not be substantially affected compared

to TLUSTY stellar atmosphere spectra in their models, even in their high mass-loss case. However, [Schaerer \(2002\)](#) also notes that for sufficiently dense winds, the He^+ flux could potentially get substantially suppressed (as demonstrated by [Chen et al. 2015](#) for metal-enriched stars). It may therefore be interesting to revisit this issue in the future, using stellar atmosphere spectra with updated wind models for Pop III stars. However, it should be noted that if winds are launched only late in the evolution of Pop III stars, this is unlikely to matter for the time-integrated emission of ionizing photons into the surrounding medium, unless the Pop III stars also exhibit high T_{eff} in such stages.

Finally, rapidly rotating stars would not be able to retain spherical shapes, and would exhibit different T_{eff} and surface gravities at their poles compared to their equators, thereby exhibiting anisotropic SEDs. While orientations would be randomized in a large population of such stars, mechanical mass-loss due to rotation may also preferentially happen in the direction perpendicular to the rotation axis, which could introduce a systematic bias in the UV emissivities seen by the surrounding interstellar and intergalactic medium, compared with the simplified models used here.

6.4 Binary Pop III stars

In this paper, we have exclusively considered models for single stars, even though Pop III stars in simulations often form binary and higher-order systems (e.g. [Stacy & Bromm 2013](#); [Sugimura et al. 2020](#)). As shown by [Tsai et al. \(2023\)](#), binary interactions can boost the UV fluxes of Pop III stars (in the case of lifetime-integrated fluxes by up to a factor of ≈ 2 in the LW band, which is the strongest effect seen in their models). However, binary interactions are also expected to affect stellar rotation rates (e.g. [de Mink et al. 2013](#)), which by themselves affect stellar evolution and consequently these fluxes. Given the many open questions regarding the stellar initial mass function, initial rotation rate and binary interactions of Pop III stars, models of the UV flux from these stars are likely to suffer from significant uncertainties until the arrival of better observational constraints. As rotation and binary interactions affect the end states of Pop III stars, such constraints may for instance come from the study of Pop III supernova yields in second generation stars or gas absorption systems, from direct observations of Pop III supernovae or gamma-ray bursts (and their afterglows), or from future gravitational wave detectors.

7 CONCLUSIONS

In this work, we have presented a set of publicly available models for the UV photon production rates of single Pop III stars, with and without rotation, across a wide range of stellar masses. We have investigated how the photon production rates are affected by the adoption of blackbody spectra compared with stellar atmosphere spectra. We have also investigated and compared the resulting lifetime-integrated emissivities of several different sets of Pop III tracks. For selected models, we also explored the potential role of stellar rotation on the equivalent width of the HeII λ 1640 emission line, on the 21-cm global signal and the spherically averaged 21-cm power spectrum.

Our conclusions can be summarized as follows:

- (i) The assumption of blackbody spectra generally overestimate He^+ ionizing rates, in some cases by more than an order of magnitude, depending on the T_{eff} of the star.
- (ii) Based on the stellar evolutionary tracks of [Yoon et al. \(2012\)](#), which take rotation and magnetic fields into account and predict

evolution to $T_{\text{eff}} > 10^5$ K at the end stages of evolution, we show that rotation significantly increases the total He^+ ionizing photon production of Pop III stars in the range 20 to $100 M_{\odot}$ compared with stars without rotation.

(iii) If gas can be retained with high-redshift Pop III systems dominated by rotating $\sim 20 M_{\odot}$ stars, then such systems may be able to produce very strong $\text{HeII}\lambda 1640$ emission with rest-frame equivalent widths comparable to or higher than systems dominated by $\geq 100 M_{\odot}$ non-rotating Pop III stars.

(iv) Differences between rotating and non-rotating Pop III stars in 21-cm observables like the 21-cm global signal and the 21-cm power spectrum are modest – of the order 20 per cent at maximum for the global signal ($z \approx 15$), and a factor of 2–3 for the ionization peak in the power spectrum ($z \approx 12.5$) – due to the extreme ionizing flux of rotating stars. These differences could be detectable in certain scenarios (such as high Pop III star-formation efficiencies, and late onset of Pop II star-formation).

(v) We highlight that two disparate values for the Lyman–Werner rates of Pop III stars have been used in the previous literature on 21-cm cosmology and high-redshift star formation ($\sim 5 \times 10^3$ vs $\sim 1 \times 10^5$ LW photons per stellar baryon). Our models favour a value around $\sim 10^4$ LW photons per stellar baryon, in line with other recent estimates (e.g. Liu et al. 2025a).

ACKNOWLEDGEMENTS

This manuscript is based on work initially conducted as part of the first author’s Master’s thesis Wasserman (2025). The work has been expanded upon and revised in collaboration with the co-authors for this publication. EZ acknowledges project grant 2022-03804 from the Swedish Research Council (Vetenskapsrådet). This work was supported in part by the International Centre for Theoretical Sciences (ICTS) for participating in the program - Radio Cosmology and Continuum Observations in the SKA Era: A Synergic View. (code: ICTS/radiocoscon2025/04).

DATA AVAILABILITY

Publicly available grids of Muspelheim models (SEDs, $Q(t)$) and both lifetime-integrated and lifetime-average photon production rates are available from: <https://www.astro.uu.se/~ez/muspelheim/muspelheim.html>

REFERENCES

Barkana R., Loeb A., 2005, *ApJ*, **626**, 1
 Bromm V., Kudritzki R. P., Loeb A., 2001, *ApJ*, **552**, 464
 Chatzikos M., et al., 2023, *Rev. Mex. Astron. Astrofis.*, **59**, 327
 Chen Y., Bressan A., Girardi L., Marigo P., Kong X., Lanza A., 2015, *MNRAS*, **452**, 1068
 Costa G., et al., 2025, *A&A*, **694**, A193
 D’Odorico V., et al., 2023, *arXiv e-prints*, p. [arXiv:2311.16803](https://arxiv.org/abs/2311.16803)
 Fialkov A., Barkana R., Visbal E., 2014, *Nature*, **506**, 197
 Fragos T., et al., 2013a, *ApJ*, **764**, 41
 Fragos T., Lehmer B. D., Naoz S., Zezas A., Basu-Zych A., 2013b, *ApJ*, **776**, L31
 Fraser M., Casey A. R., Gilmore G., Heger A., Chan C., 2017, *MNRAS*, **468**, 418
 Fujimoto S., et al., 2025, *arXiv e-prints*, p. [arXiv:2501.11678](https://arxiv.org/abs/2501.11678)
 Gessey-Jones T., et al., 2022, *MNRAS*, **516**, 841
 Gessey-Jones T., et al., 2025, *arXiv e-prints*, p. [arXiv:2502.18098](https://arxiv.org/abs/2502.18098)

Gunasekera C. M., et al., 2023, *Research Notes of the American Astronomical Society*, **7**, 246
 Hassan J., Perna R., Cantiello M., Parsotan T., Lazzati D., Walker N., 2025, *arXiv e-prints*, p. [arXiv:2505.21463](https://arxiv.org/abs/2505.21463)
 Hawcroft C., et al., 2025, *arXiv e-prints*, p. [arXiv:2505.24841](https://arxiv.org/abs/2505.24841)
 Hirano S., Bromm V., 2018, *MNRAS*, **476**, 3964
 Hubeny I., Lanz T., 1995, *ApJ*, **439**, 875
 Ishigaki M. N., Tominaga N., Kobayashi C., Nomoto K., 2018, *ApJ*, **857**, 46
 Jeena S. K., Banerjee P., Chiaki G., Heger A., 2023, *MNRAS*, **526**, 4467
 Jiang R., Zhao G., Li H., Xing Q., 2024, *ApJ*, **976**, 68
 Johnson J. L., 2010, *MNRAS*, **404**, 1425
 Kar Chowdhury R., Chang J. N. Y., Dai L., Natarajan P., 2024, *ApJ*, **966**, L33
 Klessen R. S., Glover S. C. O., 2023, *ARA&A*, **61**, 65
 Larkin M. M., Gerasimov R., Burgasser A. J., 2023, *AJ*, **165**, 2
 Lazar A., Bromm V., 2022, *MNRAS*, **511**, 2505
 Liu B., Bromm V., 2020, *MNRAS*, **497**, 2839
 Liu B., Sibony Y., Meynet G., Bromm V., 2021, *MNRAS*, **506**, 5247
 Liu B., et al., 2025a, *arXiv e-prints*, p. [arXiv:2504.00535](https://arxiv.org/abs/2504.00535)
 Liu B., Sibony Y., Meynet G., Bromm V., 2025b, *ApJ*, **980**, L30
 Maiolino R., et al., 2024, *A&A*, **687**, A67
 Martinet S., Meynet G., Ekström S., Georgy C., Hirschi R., 2023, *A&A*, **679**, A137
 Mas-Ribas L., Dijkstra M., Forero-Romero J. E., 2016, *ApJ*, **833**, 65
 Mebane R. H., Mirocha J., Furlanetto S. R., 2018, *MNRAS*, **479**, 4544
 Moriya T. J., Quimby R. M., Robertson B. E., 2022, *ApJ*, **925**, 211
 Murphy L. J., et al., 2021a, *MNRAS*, **501**, 2745
 Murphy L. J., Groh J. H., Farrell E., Meynet G., Ekström S., Tsiatsiou S., Hackett A., Martinet S., 2021b, *MNRAS*, **506**, 5731
 Nakajima K., Maiolino R., 2022, *MNRAS*, **513**, 5134
 Pober J. C., et al., 2013, *AJ*, **145**, 65
 Pober J. C., et al., 2014, *ApJ*, **782**, 66
 Pochinda S., et al., 2024, *MNRAS*, **531**, 1113
 Raiter A., Schaerer D., Fosbury R. A. E., 2010, *A&A*, **523**, A64
 Rauch T., 2003, *A&A*, **403**, 709
 Reis I., Fialkov A., Barkana R., 2021, *MNRAS*, **506**, 5479
 Sarmento R., Scannapieco E., Cohen S., 2018, *ApJ*, **854**, 75
 Schaerer D., 2002, *A&A*, **382**, 28
 Schaerer D., 2003, *A&A*, **397**, 527
 Sibony Y., Liu B., Simmonds C., Meynet G., Bromm V., 2022, *A&A*, **666**, A199
 Sodini A., et al., 2024, *A&A*, **687**, A314
 Song H., Meynet G., Li Z., Peng W., Zhang R., Zhan Q., 2020, *ApJ*, **892**, 41
 Sridhar S., Williams W., Breen S., 2024, SKA Low and Mid Subarray Templates
 Stacy A., Bromm V., 2013, *MNRAS*, **433**, 1094
 Sugimura K., Matsumoto T., Hosokawa T., Hirano S., Omukai K., 2020, *ApJ*, **892**, L14
 Tsai S.-H., Chen K.-J., Whalen D., Ou P.-S., Woods T. E., 2023, *ApJ*, **951**, 84
 Tsiatsiou S., et al., 2024, *A&A*, **687**, A307
 Tumlinson J., Shull J. M., 2000, *ApJ*, **528**, L65
 Vanni I., Salvadori S., D’Odorico V., Becker G. D., Cupani G., 2024, *ApJ*, **967**, L22
 Vanzella E., et al., 2023, *A&A*, **678**, A173
 Venditti A., Graziani L., Schneider R., Pentericci L., Di Cesare C., Maio U., Omukai K., 2023, *MNRAS*, **522**, 3809
 Venditti A., Bromm V., Finkelstein S. L., Graziani L., Schneider R., 2024, *MNRAS*, **527**, 5102
 Ventura E. M., Qin Y., Balu S., Wyithe J. S. B., 2025, *arXiv e-prints*, p. [arXiv:2502.08971](https://arxiv.org/abs/2502.08971)
 Volpato G., Marigo P., Costa G., Bressan A., Trabucchi M., Girardi L., 2023, *ApJ*, **944**, 40
 Volpato G., Marigo P., Costa G., Bressan A., Trabucchi M., Girardi L., Addari F., 2024, *ApJ*, **961**, 89
 Wang X., et al., 2024, *ApJ*, **967**, L42
 Wasserman J., 2025, The high-redshift signatures of Population III stars, Master’s thesis, Uppsala University, forthcoming
 Windhorst R. A., et al., 2018, *ApJS*, **234**, 41
 Yoon S. C., Dierks A., Langer N., 2012, *A&A*, **542**, A113

Yoshii Y., Sameshima H., Tsujimoto T., Shigeyama T., Beers T. C., Peterson B. A., 2022, [ApJ](#), **937**, 61
 Zackrisson E., et al., 2012, [MNRAS](#), **427**, 2212
 Zackrisson E., et al., 2024, [MNRAS](#), **533**, 2727
 de Mink S. E., Langer N., Izzard R. G., Sana H., de Koter A., 2013, [ApJ](#), **764**, 166

APPENDIX A: EXTRA TABLES AND FIGURES

Table A1 shows the average lifetime photon production rates for the Yoon et al. (2012) and Murphy et al. (2021a) models used in this work. Fig. A1 shows the neutral fractions from the 21cmSPACE simulations in Fig. 7.

This paper has been typeset from a \LaTeX file prepared by the author.

Table A1. Average lifetime photon production rates. The first column is the model source, the second gives the initial rotational velocity in fraction of the Keplerian velocity for Yoon et al. (2012) and critical velocity for Murphy et al. (2021a). The third column is the ZAMS mass in solar masses, the fourth through eighth column is the logarithm of the average lifetime photon production rates [s^{-1}] for the respective energy ranges, and the last column is the lifetimes in years.

| Source | Rotation | Mass | \bar{Q}_H | \bar{Q}_{He} | \bar{Q}_{He+} | \bar{Q}_{LW} | \bar{Q}_{Ly} | Lifetime |
|-----------|----------|------|-------------|----------------|-----------------|----------------|----------------|----------|
| Yoon+12 | 0.0 | 10 | 47.71 | 47.23 | 41.98 | 47.57 | 47.75 | 2.61E+07 |
| Yoon+12 | 0.0 | 20 | 48.66 | 48.31 | 43.79 | 48.20 | 48.37 | 1.02E+07 |
| Yoon+12 | 0.0 | 30 | 49.10 | 48.77 | 44.87 | 48.54 | 48.70 | 6.81E+06 |
| Yoon+12 | 0.0 | 60 | 49.68 | 49.39 | 47.66 | 49.00 | 49.17 | 4.16E+06 |
| Yoon+12 | 0.0 | 100 | 50.02 | 49.74 | 48.54 | 49.29 | 49.46 | 3.27E+06 |
| Yoon+12 | 0.0 | 150 | 50.27 | 50.00 | 48.98 | 49.54 | 49.71 | 2.70E+06 |
| Yoon+12 | 0.0 | 200 | 50.40 | 50.14 | 49.19 | 49.66 | 49.83 | 2.64E+06 |
| Yoon+12 | 0.0 | 300 | 50.59 | 50.33 | 49.45 | 49.85 | 50.01 | 2.40E+06 |
| Yoon+12 | 0.0 | 500 | 50.83 | 50.57 | 49.73 | 50.08 | 50.25 | 2.18E+06 |
| Yoon+12 | 0.4 | 10 | 47.56 | 46.98 | 41.53 | 47.57 | 47.75 | 2.74E+07 |
| Yoon+12 | 0.4 | 20 | 48.88 | 48.63 | 47.48 | 48.12 | 48.28 | 1.52E+07 |
| Yoon+12 | 0.4 | 30 | 49.26 | 49.03 | 48.00 | 48.40 | 48.56 | 9.51E+06 |
| Yoon+12 | 0.4 | 60 | 49.79 | 49.59 | 48.75 | 48.82 | 48.98 | 5.28E+06 |
| Yoon+12 | 0.4 | 100 | 50.12 | 49.94 | 49.21 | 49.10 | 49.26 | 3.93E+06 |
| Yoon+12 | 0.4 | 150 | 50.36 | 50.18 | 49.48 | 49.32 | 49.47 | 3.28E+06 |
| Yoon+12 | 0.4 | 200 | 50.52 | 50.32 | 49.59 | 49.54 | 49.69 | 2.97E+06 |
| Yoon+12 | 0.4 | 300 | 50.69 | 50.48 | 49.68 | 49.74 | 49.90 | 2.55E+06 |
| Yoon+12 | 0.4 | 500 | 50.87 | 50.62 | 49.74 | 50.07 | 50.25 | 2.23E+06 |
| Murphy+21 | 0.0 | 9 | 47.68 | 47.13 | 43.98 | 47.30 | 47.61 | 2.00E+07 |
| Murphy+21 | 0.0 | 12 | 48.10 | 47.63 | 44.86 | 47.48 | 47.83 | 1.93E+07 |
| Murphy+21 | 0.0 | 15 | 48.23 | 47.90 | 45.47 | 47.55 | 48.01 | 1.40E+07 |
| Murphy+21 | 0.0 | 20 | 48.84 | 48.40 | 46.19 | 48.07 | 48.26 | 1.03E+07 |
| Murphy+21 | 0.0 | 30 | 49.07 | 48.82 | 46.95 | 47.91 | 48.58 | 6.64E+06 |
| Murphy+21 | 0.0 | 40 | 49.45 | 49.16 | 47.40 | 47.87 | 48.81 | 5.21E+06 |
| Murphy+21 | 0.0 | 60 | 49.81 | 49.52 | 47.94 | 48.34 | 49.09 | 4.03E+06 |
| Murphy+21 | 0.0 | 85 | 50.15 | 49.79 | 48.37 | 49.31 | 49.34 | 3.40E+06 |
| Murphy+21 | 0.0 | 120 | 50.38 | 50.02 | 48.72 | 49.60 | 49.54 | 3.05E+06 |
| Murphy+21 | 0.4 | 9 | 47.57 | 47.06 | 41.73 | 47.47 | 47.65 | 2.38E+07 |
| Murphy+21 | 0.4 | 12 | 47.93 | 47.52 | 42.42 | 47.74 | 47.92 | 2.25E+07 |
| Murphy+21 | 0.4 | 15 | 48.26 | 47.89 | 43.02 | 47.94 | 48.11 | 1.65E+07 |
| Murphy+21 | 0.4 | 20 | 48.64 | 48.30 | 43.73 | 48.18 | 48.34 | 1.19E+07 |
| Murphy+21 | 0.4 | 30 | 49.09 | 48.77 | 44.77 | 48.49 | 48.65 | 7.60E+06 |
| Murphy+21 | 0.4 | 40 | 49.36 | 49.05 | 45.92 | 48.70 | 48.86 | 5.76E+06 |
| Murphy+21 | 0.4 | 60 | 49.70 | 49.39 | 47.50 | 49.01 | 49.18 | 4.41E+06 |
| Murphy+21 | 0.4 | 85 | 49.94 | 49.64 | 48.20 | 49.24 | 49.41 | 3.60E+06 |
| Murphy+21 | 0.4 | 120 | 50.17 | 49.89 | 48.65 | 49.43 | 49.59 | 3.14E+06 |

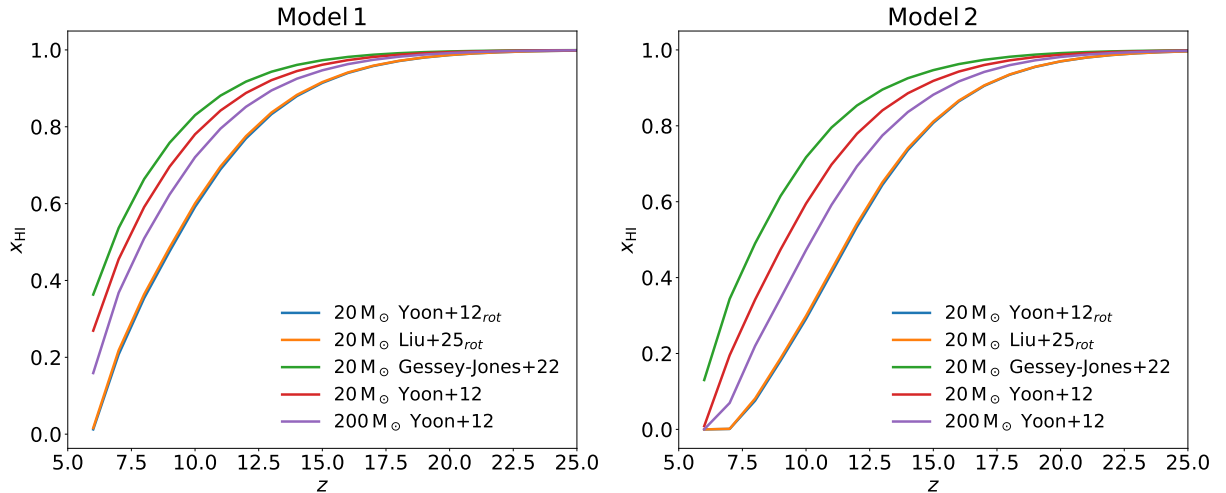


Figure A1. Neutral hydrogen fractions as a function of redshift for the 21cmSPACE simulations models included in Fig. 7. For the rotational stellar models in scenario 2, the Universe is already ionized to $x_{HI} \approx 0.8$ by $z \approx 15$.